Phase-field lattice Boltzmann equation for wettable particle fluid dynamics

Lin Zheng,[1] Song Zheng,[2,*] and Qinglan Zhai[3]

[1]*MIIT Key Laboratory of Thermal Control of Electronic Equipment, School of Energy and Power Engineering, Nanjing University of Science and Technology, Nanjing 210094, People's Republic of China*

[2]*School of Mathematics and Statistics, Zhejiang University of Finance and Economics, Hangzhou 310018, People's Republic of China*

[3]*School of Economics Management and Law, Chaohu University, Chaohu 238000, People's Republic of China*

(Received 12 August 2022; revised 13 May 2023; accepted 11 July 2023; published 7 August 2023)

In this paper a phase-field based lattice Boltzmann equation (LBE) is developed to simulate wettable particles fluid dynamics together with the smoothed-profile method (SPM). In this model the evolution of a fluid-fluid interface is captured by the conservative Allen-Cahn equation (CACE) LBE, and the flow field is solved by a classical incompressible LBE. The solid particle is represent by SPM, and the fluid-solid interaction force is calculated by direct force method. Some benchmark tests including a single wettable particle trapped at the fluid-fluid interface without gravity, capillary interactions between two wettable particles under gravity, and sinking of a horizontal cylinder through an air-water interface are carried out to validate present CACE LBE for fluid-fluid-solid flows. Raft sinking of multiple horizontal cylinders (up to five cylinders) through an air-water interface is further investigated with the present CACE LBE, and a nontrivial dynamics with an unusual nonmonotonic motion of the multiple cylinders is observed in the vertical plane. Numerical results show that the predictions by the present LBE are in good agreement with theoretical solutions and experimental data.

DOI: 10.1103/PhysRevE.108.025304

I. INTRODUCTION

Multiphase flow of two immiscible fluids is frequently observed in many natural and industrial processes such as raindrops on the ground, gas-liquid or liquid-liquid two-phase fluids in cooling systems, and enhanced oil recovery. The imbalance of microscopic interaction of molecules between different fluid phases generates a surface tension force along the fluid-fluid interface. Due to the competition of the surface tension force, viscous force, gravity force, and so on, it is still a challenging task to correctly capture the complex of transient morphological change of a fluid-fluid interface. When a wettable solid structure is involved in the immiscible fluid system, various solid structure hydrodynamics behaviors will be observed as the result of different force interactions at fluid-fluid-solid interfaces. When the characteristic length of the solid structure is much larger than the capillary length, the surface tension force can be negligible in comparison with viscous force, gravity force on the solid. On the other hand, when the characteristic length is much smaller than the capillary length, the surface force will play a crucial role in the wettable solid structure fluid dynamic of the multiphase system.

For the fluid-fluid interface capturing, some numerical methods were developed to investigate interfacial dynamics such as the front-tracking method [1], level set (LS) method [2], volume of fluid (VOF) method [3], and diffuse interface method [4]. Due to an artificial interface rupture based upon some *ad hoc* criteria [1], the front-tracking method is not suitable for simulating multiphase fluids with interface breaking and coalescing, while the VOF and LS methods require interface reconstruction or reinitialization to represent the interface at each time increment, which may introduce some unphysical results. In comparison with front tracking, LS, and VOF methods, the diffuse interface method is an implicit interface capturing over the sharp interface method, where the phase interface is treated as a finite thickness transition layer, and the physical properties of fluids vary continuously through the interfacial transition layer but with almost uniform values in the bulk regions. As one of the diffuse interface methods, the lattice Boltzmann equation (LBE) method has obtained successful applications to multiphase flow [5–19]. In the literature, pervious works demonstrated that the Allen-Cahn equation (ACE) based LBE could give a good satisfactory result for interface capturing [15–18]. Recently we proposed a generalized conservative ACE (CACE) for N immiscible fluids, and a LBE solver was designed accordingly [20,21]. The results showed the accuracy and capability of CACE-LBE for N immiscible fluids with large density contrast.

When a solid structure is immersed into the fluid, the fluid-solid boundary should be represented properly. In the LBE community, the bounce-back scheme (BBS) is frequently applied to the fluid-solid boundary [22]. In Ref. [22] Ladd proposed a half-way BBS for simulating particle suspension, and a momentum exchange method was designed to evaluate hydrodynamic force arising from the fluid-solid interaction; the results showed that this simple boundary treatment and fluid-solid interaction force calculation could give a satisfied prediction. However, this type of boundary treatment leads to a zigzag boundary in the simulation, and the zigzag boundary further causes a fluctuation in the fluid-solid interaction

*szh070318@zufe.edu.cn

during the motion of solid structure [23]. To improve the accuracy, some interpolated-bounce-back schemes were also proposed [24,25]. Alternatively, the smoothed-profile-method (SPM) was developed to represent the fluid-solid boundary [26], where an index function is used to capture the shape of particles. In fact, the SPM can be viewed as one type of diffuse interface method, where the sharp change of solid boundary is presented by a finite thickness smoothed layer. With this treatment, the limitations of a zigzag boundary presentation and fluctuation fluid-solid interaction in BBS are eliminated by SPM-LBE [27]. Moreover, the SPM-LBE has been successfully applied to simulate the particle fluid dynamics [27–29]. On the other hand, a diffuse-interface LBE for the particle-fluid interaction was proposed [30]. The two types of LBEs apply a diffuse-interface method to represent the fluid-particle interaction, but with different force treatment to incorporate fluid-particle interaction to the LBE. Recently the SPM-LBE was extended to investigate the particle trapped at the fluid-fluid interface [31,32]. In Ref. [31] Mino *et al.* applied the combination of SPM and free-energy based LBE to study a wettable particle trapped at the fluid interface under gravity. In Ref. [32] the ternary fluid color-gradient LBE was extended to model the two immiscible fluids involving solid particles by coupling with the SPM. However, the property of two immiscible fluids in their simulations was limited to matched density [31,32].

With the aforementioned reviews, in this work we will investigate the particle hydrodynamics in a two immiscible fluids system with large fluid density contrast within the framework of the SPM. To this end, we develop the CACE-LBE with the SPM to study the particle-fluid-fluid three-phase hydrodynamics. The rest of this paper is organized as follows: In Sec. II the SPM is briefly introduced, and the CACE-LBE is applied to the flow field and interface capturing in Sec. III, Some tests are carried out to show the capability of CACE-LBE for particle hydrodynamics with large fluid density contrast in Sec. IV, and finally a brief conclusion is given in Sec. V.

II. MULTIPHASE FLOW WITH SOLID PARTICLE BY THE SPM

The SPM was first proposed to resolve particle hydrodynamic interactions in an incompressible single-phase fluid [26]. In this method the original sharp solid-fluid interface between solid particle and the fluid was represented by a smoothed interface with a finite thickness D_p, where a smoothed index function ϕ_p is used to distinguish solid and fluid regions, i.e., in the fluid region, $\phi_p = 0$, while $\phi_p = 1$ in the solid region and it smoothly changes through the fluid-solid interface. With this treatment, the solid-fluid boundary can be smoothly captured. In this work, the following hyperbolic function is used:

$$\phi_p(\boldsymbol{x}) = \frac{1}{2} + \frac{1}{2}\tanh\left(2\frac{R_p - |\boldsymbol{x} - \boldsymbol{x}_p|}{D_p}\right), \tag{1}$$

where $\boldsymbol{x}$ is a local position in space, R_p is radius of solid particle, and $\boldsymbol{x}_p$ is the mass center of the solid particle.

The translational and rotational motions of circular or spherical particle can be derived by

$$M_p\frac{d\boldsymbol{V}_p}{dt} = \boldsymbol{F}_h + \boldsymbol{F}_p + \boldsymbol{F}_g, \tag{2}$$

$$\boldsymbol{I}_p \cdot \frac{d\boldsymbol{\Omega}_p}{dt} = \boldsymbol{T}_h, \tag{3}$$

where M_p, $\boldsymbol{V}_p$, $\boldsymbol{\Omega}_p$, and $\boldsymbol{I}_p$ are the mass, translational velocity, angular velocity, and inertial tensor of the particle, respectively. $\boldsymbol{F}_h$ and $\boldsymbol{T}_h$ are the hydrodynamic force and torque. $\boldsymbol{F}_p$ is the particle-particle interaction force. $\boldsymbol{F}_g$ is the force arising from the gravitational and buoyant forces as $\boldsymbol{F}_g = M_p(1 - \rho/\rho_p)\boldsymbol{g}$, where ρ and ρ_p are the density of the ambient fluid and particle, respectively, and $\boldsymbol{g}$ is the gravitational acceleration.

In Eq. (2) the key point is to compute the hydrodynamic force $\boldsymbol{F}_h$. There are several types of methods proposed for evaluating $\boldsymbol{F}_h$ such as the momentum exchange method [22,33], stress integration method [34], and direct force method [26,27]. As mentioned in the previous section, the momentum exchange method can cause a fluctuation of the fluid-solid interaction [23]. The stress integration method has a complex extrapolation operation to calculate the stress tensor along the surface of the particle, which may induce more instability issues, while the direct force method simply evaluates the force on the forcing point to satisfy the nonslip boundary condition. Once the hydrodynamic force $\boldsymbol{F}_h$ is obtained, the hydrodynamic torque $\boldsymbol{T}_h$ can be computed, and then the translational and angular velocities are updated by Eqs. (2) and (3). One merit of SPM is the calculation of the hydrodynamic interaction force $\boldsymbol{F}_h$ on the particle as one of the direct force methods, which can be obtained by the summation of the fluid-solid interaction force $\boldsymbol{f}_p$ at the position $\boldsymbol{x}$. Therefore, we need to determine the local value of $\boldsymbol{f}_p$. Actually, in a time interval δt, it can be uniformly expressed by the following equation [26,27]:

$$\boldsymbol{f}_p(\boldsymbol{x}, t) = \phi_p(\boldsymbol{x}, t)\rho(\boldsymbol{x}, t)[\boldsymbol{u}^*(\boldsymbol{x}, t) - \boldsymbol{u}_p(\boldsymbol{x}, t)]/\delta t, \tag{4}$$

where $\boldsymbol{u}^*$ is an intermediate velocity of the fluid without the effect of solid particle, and $\boldsymbol{u}_p$ is the particle velocity defined by

$$\boldsymbol{u}_p = \boldsymbol{V}_p + \boldsymbol{\Omega}_p \times (\boldsymbol{x} - \boldsymbol{x}_p). \tag{5}$$

Then the hydrodynamic force and torque can be simply computed by [26,27]

$$\boldsymbol{F}_h = \sum_{\boldsymbol{x}} \boldsymbol{f}_p(\boldsymbol{x}, t), \tag{6}$$

$$\boldsymbol{T}_h = \sum_{\boldsymbol{x}} (\boldsymbol{x} - \boldsymbol{x}_p) \times \boldsymbol{f}_p(\boldsymbol{x}, t). \tag{7}$$

When the solid particle immerses into two immiscible fluids, the hydrodynamic transport phenomena of the immiscible fluids should be correctly captured. Due to the explicit expression of the pressure tensor, surface tension force, and chemical potential in phase-field theory, the phase-field theory-based method has received considerable attention [11,12,14,31–33]. In this theory, the fluid-fluid interface of two immiscible fluids is assumed to have a finite thickness, and the fluid properties

are changed smoothly through the interface region. One of the important points in phase-field theory is the explicit form of the mixed free energy E functional for the multiphase fluid system, which can derive the fluid quantities such as the chemical potential by the model parameters in E as an example. In this work the following mixture of free energy is used to model the two-phase flow system, which can be written by [4]

$$E = \int \left[E_0 + \frac{\kappa}{2}|\nabla c|^2 \right] d\Omega, \tag{8}$$

where E_0 is a bulk free energy, which is often approximated by $E_0(c) = \beta c^2(c-1)^2$ with β as a model parameter. κ is a gradient coefficient related to fluid surface tension σ and interface thickness D. c is an order parameter, i.e., $c = 0$ in one fluid region while $c = 1$ in another fluid region. The relation between β, κ, D, and σ can be written as

$$\beta = \frac{12\sigma}{D}, \quad \kappa = \frac{3D\sigma}{2}. \tag{9}$$

In the literature, the evolution of the order parameter c is governed by the well-known Cahn-Hilliard equation (CHE) [35] or ACE [36], and these two types of interface-capturing methods obtain successful applications in two-phase or multicomponent immiscible fluids. In the CHE, the driven force is proportional to the gradient of chemical potential, where it is complicated to design a compact and efficient discretization scheme for the fourth-order gradients, whereas only second-order derivatives appeared in ACE and make it much simpler for discretization. Therefore, one of the ACEs, i.e., the CACE, is used for interface capturing in the present work, which can be written by [37]

$$\partial_t c + \nabla \cdot (c\boldsymbol{u}) = \nabla \cdot \left\{ M \left[\nabla c - \frac{4c(c-1)}{D} \boldsymbol{n} \right] \right\}, \tag{10}$$

where $\boldsymbol{u}$ is fluid velocity, M is the mobility, and $\boldsymbol{n} = \nabla c/|\nabla c|$ is an outward pointing unit normal vector.

When the CACE is coupled with velocity field, the hydrodynamic equation for the incompressible immiscible fluids can be written by

$$\nabla \cdot \boldsymbol{u} = 0, \tag{11}$$

$$\partial_t(\rho \boldsymbol{u}) + \nabla \cdot (\rho \boldsymbol{u}\boldsymbol{u}) = -\nabla p + \nabla \cdot \boldsymbol{S} + \boldsymbol{F}, \tag{12}$$

where p is the hydrodynamic pressure, and $\boldsymbol{S} = \eta(\nabla \boldsymbol{u} + \boldsymbol{u}\nabla)$ is the viscous stress term with η as dynamic viscosity. $\boldsymbol{F} = \mu \nabla c - \boldsymbol{F}_h$ is the interface force minus hydrodynamic force on the particle; here μ is the chemical potential, and it can be derived by the variational derivative of mixing free energy with respect to the order parameter c, that is, $\mu = \delta E/\delta c = \mu_0 - \kappa \nabla^2 c$ with $\mu_0 = \partial E_0/\partial c$ as the bulk chemical potential.

III. LBE FOR HYDRODYNAMICS AND INTERFACE CAPTURING

A. LBE for hydrodynamic equations

The hydrodynamic equations of Eqs. (11) and (12) can be solved by a two-phase LBE. In the model, the evolution of incompressible fluid flow can be achieved by introducing a density distribution function f_i, and its evolution equation can be derived by [7,10,14]

$$\begin{aligned} &f_i(\boldsymbol{x} + \boldsymbol{\xi}_i \delta t, t + \delta t) - f_i(\boldsymbol{x}, t) \\ &= -\frac{1}{\tau_f}\left(f_i - f_i^{(\mathrm{eq})}\right) + \delta t \left(1 - \frac{1}{2\tau_f}\right)\{\boldsymbol{F} \cdot (\boldsymbol{\xi}_i - \boldsymbol{u})\Gamma_i(\boldsymbol{u}) \\ &\quad + (\boldsymbol{\xi}_i - \boldsymbol{u}) \cdot \nabla\left(\rho c_s^2\right)[\Gamma_i(\boldsymbol{u}) - \Gamma_i(0)]\}, \end{aligned} \tag{13}$$

where $\boldsymbol{\xi}_i$ is molecular velocity, δt is time increment, τ_f is single relaxation time, and $f_i^{(\mathrm{eq})}$ is defined by

$$f_i^{(\mathrm{eq})} = \omega_i \left\{ p + \rho c_s^2 \left[\frac{\boldsymbol{\xi}_i \cdot \boldsymbol{u}}{c_s^2} + \frac{1}{2}\left(\left(\frac{\boldsymbol{\xi}_i \cdot \boldsymbol{u}}{c_s^2} \right)^2 - \frac{\boldsymbol{u}^2}{c_s^2} \right) \right] \right\}, \tag{14}$$

with ω_i as the weight coefficient and c_s as sound speed. $\Gamma_i(\boldsymbol{u})$ is given by

$$\Gamma_i(\boldsymbol{u}) = \omega_i \left\{ 1 + \frac{\boldsymbol{\xi}_i \cdot \boldsymbol{u}}{c_s^2} + \frac{1}{2}\left[\left(\frac{\boldsymbol{\xi}_i \cdot \boldsymbol{u}}{c_s^2} \right)^2 - \frac{\boldsymbol{u}^2}{c_s^2} \right] \right\}, \tag{15}$$

The dynamic pressure and velocity of fluid can be calculated by the zeroth and first velocity moments of f_i, respectively, which are given by

$$p = \sum_i f_i + \frac{\delta t}{2} \boldsymbol{u} \cdot \nabla \rho c_s^2, \quad \rho c_s^2 \boldsymbol{u} = \sum_i \boldsymbol{\xi}_i f_i + \frac{\delta t}{2} \boldsymbol{F}, \tag{16}$$

and the value of τ can be determined by η through the relation $\eta = \rho(\tau_f - 1/2)c_s^2 \delta t$.

B. CACE LBE solver

In the past decades, two types of phase-field theory-based LBE were developed for interface capturing: one was CHE-based LBE; another was ACE-based LBE. Recently CACE-based LBE as one of the ACE LBEs has received particular attention on athermal two-phase flow. Compared with CHE-based LBE, numerical results demonstrated that CACE-based LBE could give more efficient and less dispersive for interface capturing with large density contrast. Therefore, the CACE-based LBE is used for interface capturing, and its evolution equation can be given as [14,38]

$$\begin{aligned} &h_i(\boldsymbol{x} + \boldsymbol{\xi}_i \delta t, t + \delta t) - h_i(\boldsymbol{x}, t) \\ &= -\frac{1}{\tau_h}(h_i - h_i^{(\mathrm{eq})}) + \delta t \left(1 - \frac{1}{2\tau_h}\right) S_i, \end{aligned} \tag{17}$$

where τ_h is single relaxation time, $h_i^{(\mathrm{eq})}$ is the equilibrium distribution function, which is defined by

$$h_i^{(\mathrm{eq})} = \omega_i \left\{ H_i + c \left[\frac{\boldsymbol{\xi}_i \cdot \boldsymbol{u}}{c_s^2} + \frac{1}{2}\left(\left(\frac{\boldsymbol{\xi}_i \cdot \boldsymbol{u}}{c_s^2} \right)^2 - \frac{\boldsymbol{u}^2}{c_s^2} \right) \right] \right\}, \tag{18}$$

with

$$H_i = \begin{cases} [c - (1-\omega_0)\Gamma_h c]/\omega_0, & i = 0, \\ \Gamma_h c, & i > 0, \end{cases} \tag{19}$$

and Γ_h is an adjustable parameter. The source term S_i in Eq. (17) is defined by

$$S_i = \omega_i \Gamma_h \boldsymbol{\xi}_i \cdot \boldsymbol{s}, \tag{20}$$

where $\boldsymbol{s} = 4c(c-1)\boldsymbol{n}/D$.

With Eqs. (17)–(20), c can be updated and calculated by summation of the distribution function h_i as

$$c = \sum_i h_i, \tag{21}$$

and the relation between mobility M and τ_h can be given by $M = \Gamma_h(\tau_h - 1/2)c_s^2\delta t$.

When a wettable particle immerses into the two immiscible fluids, the wettability boundary condition for the particle should be properly implemented. Similar to Ref. [39], in this work a uniform value of c_w imposed at the particle can be used to tune the particle's wettability, and its value varies from 0 to 1. Obviously, the neutral wetting particle can be realized by setting $c_w = 0.5$. However, the free energy in Eq. (8) shows that it is a two-well profile with two minimums at $c = 0, 1$. Therefore, the diffusion between the solid and surrounding fluids appears with such a wettability boundary condition when the wettable particle immerses into two immersible fluids. To suppress this effect, the following treatment is added to the source term S_i at the interface region Ω_{int} in Eq. (17)

$$S_{m,i} = \frac{\int_{\Omega_f}(c_0 - c)d\Omega}{\int_{\Omega_{\text{int}}} d\Omega}\Gamma_i(\boldsymbol{u}), \tag{22}$$

where c_0 is the initial value of order parameter c at fluid domain Ω_f, and Ω_{int} is the interface region. In Eq. (22) the numerator $\int_{\Omega_f}(c_0 - c)d\Omega$ represents the total change of c in comparison with its initial value c_0 in Ω_f, and the denominator $\int_{\Omega_{\text{int}}} d\Omega$ represents the fluid-fluid interface region, where the value of c varies from 0.1 to 0.9 in this work. Therefore, the ratio between the two integrals means that the total change of c is uniformly distributed at the fluid-fluid interface region. To implement the wettability of the solid particle, the direct force method used in Eq. (10) can be similarly applied to realize the desired value of c_w at the particle, which can be achieved by adding a source term $S_{c,i}$ to Eq. (17):

$$S_{c,i} = \omega_i \phi_p (c_w - c). \tag{23}$$

With this modification, the value of c inside the particle is replaced by c_w, i.e., the current order parameter $\bar{c}$ should be modified by $\bar{c} = c + \phi_p(c_w - c)$, where $\bar{c} = c$ in the fluid region with $\phi_p = 0$, and $\bar{c} = c_w$ in the solid particle region with $\phi_p = 1$.

In Eqs. (13), (16), (17), and (20), the gradient terms appear in the force and source terms and the calculations of fluid quantities, therefore, the spatial discretization should be properly used to evaluate their values. In this work the following second-order isotropic schemes are applied to discretize the gradient and the Laplacian operators [40]:

$$\nabla\phi(\boldsymbol{x}, t) = \sum_k \frac{w_k \boldsymbol{\xi}_k \phi(\boldsymbol{x} + \boldsymbol{\xi}_k \delta t, t)}{c_s^2 \delta t}, \tag{24}$$

$$\nabla^2\phi(\boldsymbol{x}, t) = \sum_k \frac{2w_k[\phi(\boldsymbol{x} + \boldsymbol{\xi}_k \delta t, t) - \phi(\boldsymbol{x}, t)]}{c_s^2 \delta t^2}, \tag{25}$$

where ϕ is any physical variable.

It should be pointed out that Mino and Shinto proposed a free-energy-based LBE for the wettable particle trapped at the fluid-fluid interface [31]. In their work a modified free energy including the solid particle wettability parameter and a sufficiently large value of the artificial parameter is applied to enforce the same value of order parameter inside the solid particle as the desired solid particle wettability. Nevertheless, the two immiscible fluids in the particle-fluid-fluid multiphase system are limited to matched density. However, the standard free energy of a two-phase flow system used in the literature is applied without modification in the present work, and the wettability of the particle is realized by Eq. (23). Due to this simple treatment, the wettability of the particle becomes a source of the order parameter in the particle-fluid-fluid multiphase system. To suppress this effect, the source term of Eq. (22) is designed and added to Eq. (17). Moreover, with such a treatment, the particle-fluid-fluid system is not limited to the matched fluid density but with a large density contrast by the present LBE.

IV. NUMERICAL SIMULATIONS

In this section some benchmark problems such as a wettable cylindrical particle trapped at the fluid-fluid interface, capillary interactions between two wettable cylindrical particles, and sinking of a horizontal cylinder or multiple horizontal cylinders through an air-water interface are carried out to validate the present CACE LBE coupled with the SPM for particle hydrodynamics in two immiscible fluids system, where the numerical results predicted by the present work are compared with the analytical solutions and/or available data. In the following simulation, the standard two-dimensional nine discrete velocities model is applied to present CACE LBE with ω_i given as $\omega_0 = 4/9$, $\omega_{1-4} = 1/9$, and $\omega_{5-8} = 1/36$, and the nondimensional quantities such as density ratios, $\rho_k = \tilde{\rho}_k/\tilde{\rho}_r$, and viscosity ratios, $\eta_k = \tilde{\eta}_k/\tilde{\eta}_r$ are used, where $\tilde{\rho}_k$ and $\tilde{\eta}_k$ are the physical density and viscosity of the kth phase with $k = l$ (liquid) or g (gas), and $\tilde{\rho}_r$ and $\tilde{\eta}_r$ are the reference density, viscosity, respectively. Without being otherwise specified, some model parameters are set by $D = 5$, $D_p = 2$, and $M = 0.1$.

A. A wettable cylindrical particle on fluid-fluid interface

A wettable cylindrical particle trapped at the fluid-fluid interface without gravity force is a good test to show the accuracy and capability of the present CACE LBE for simulating particle-fluid-fluid flow. In this problem, the physical domain $x \times y = [-L/2, L/2] \times [-L/2, L/2]$ is divided into two layers with a periodic boundary in the x direction and nonslip boundary conditions at other wall boundaries, that is, the upper layer of the domain $(0 < y \leqslant L/2)$ is filled with one fluid, and the lower layer $(-L/2 \leqslant y < 0)$ is filled with another fluid. In the upper layer, the fluid properties are set as density ρ_g, viscosity η_g, while the fluid properties of density ρ_l, viscosity η_l are imposed in the lower layer. Initially, the mass center of cylindrical particle with radius R_p and mass density ρ_p is located at the center of the physical domain. Due to the interaction of the fluid-solid particle, the balance of the

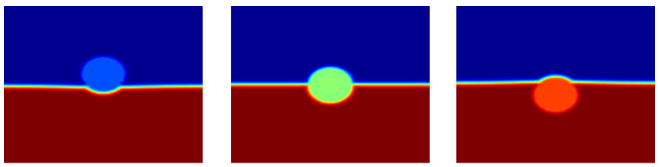

FIG. 1. Snapshots of mechanical equilibrium state for single wettable particle trapped at the fluid-fluid interface without gravity. (a) $\chi = 0.2$, (b) $\chi = 0.5$, and (c) $\chi = 0.8$.

capillary force from the fluid-fluid and fluid-solid determines the equilibrium state of the particle, where the equilibrium position of particle $h^{\rm eq}$ (the distance from the fluid-fluid interface to particle center) can be obtained similarly as Ref. [39] by

$$\cos\theta = \frac{h^{\rm eq}}{R_p} = \frac{\sigma_{pg} - \sigma_{pl}}{\sigma_{lg}} = (2\chi - 1)\big(1 - 2\chi^2 + 2\chi\big), \tag{26}$$

where θ is the contact angle, and σ_{pl} and σ_{pg} are respectively the interfacial tension between the particle and fluid. χ is an affinity parameter related to the wettability of the particle, which can be determined by c_w, namely, $\chi = c_w$. Therefore, the change of χ can achieve a wide range of the particle's wettability, and it can further affect the wetting behavior of the particle.

In the simulation, the computational domain is divided into a 150×150 mesh. The physical properties of two fluids are chosen as $\sigma_{lg} = 1.0 \times 10^{-2}$, $\rho_l = 1.0$, $\rho_g = 0.001$, $\eta_l/\eta_g = 1.0$, the mass density of solid particle with $R_p = 15$ is given by $\rho_p = 1.2$, and the relaxation times are set by $\tau_f = \tau_h = 1.0$. In Fig. 1 the equilibrium state of the wettable cylindrical particle trapped at the fluid-fluid interface is presented by the effect of affinity parameter χ on the wetting behavior of the particle. It is shown that the particle immerses into the gas phase with a small value of $\chi < 0.5$ while it enters into the liquid phase with a large value of $\chi > 0.5$. For the neutral wetting particle ($\chi = 0.5$), the solid particle keeps the initial location at the fluid-fluid interface. Numerical predictions also show that the wettability effect of the particle on the particle behavior is qualitatively captured by the present LBE. For the quantitative comparison, we further compare the numerical predictions of the equilibrium position of the particle with the theoretical results predicted by Eq. (26). In Fig. 2 the effect of the affinity parameter χ on the normalized equilibrium position $\cos\theta =$

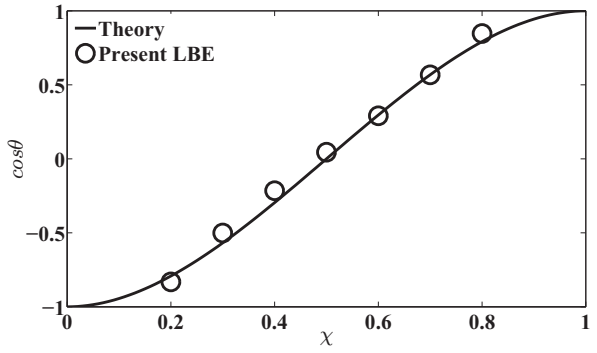

FIG. 2. Comparison of $\cos\theta = h/R_p$ as a function of χ between the present LBE and theory by Eq. (26).

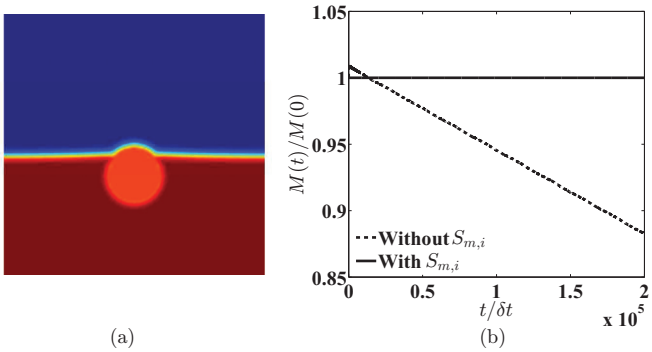

FIG. 3. Results of a single wettable cylindrical particle ($\chi = 0.8$) trapped at the fluid-fluid interface without gravity. (a) Snapshot of the single wettable cylindrical particle trapped at the fluid-fluid interface by the present LBE without $S_{m,i}$ at $t = 2 \times 10^5 \delta t$. (b) Comparison of $M(t)/M(0)$ vs t between the present LBE with and without $S_{m,i}$.

$h^{\rm eq}/R_p$ is presented. It is shown that the present numerical predictions agree with the analytical solutions, and further demonstrated that the wetting behavior of the solid particle is well simulated and captured by the present LBE with large fluid density contrast.

In Fig. 3 the effect of the remedial term $S_{m,i}$ in Eq. (22) is investigated by the present LBE with $\chi = 0.8$ as an example. It can be observed that the region of the liquid phase becomes less at $t = 2 \times 10^5 \delta t$ by the present LBE without $S_{m,i}$ as shown in Fig. 3(a), while the result of the mechanical equilibrium state in Fig. 1(c) shows the present LBE with $S_{m,i}$ is free of this issue. To give a quantitative comparison, we measure the transient total volume fraction $M(t) = \int_{\Omega_f} c d\Omega$ for the present LBE with and without $S_{m,i}$, and the ratio between $M(t)$ and $M(0)$ is plotted in Fig. 3(b). The results show that the ratio $M(t)/M(0)$ is first increased and then reduced with the time t by the present LBE without $S_{m,i}$. When $S_{m,i}$ is considered by the present LBE, the initial value of $M(0)$ is well maintained. Therefore, the remedial term $S_{m,i}$ should be included in Eq. (17).

B. Capillary interactions between two wettable cylindrical particles

Capillary interactions between two wettable cylindrical particles in the presence of gravity are another good test to demonstrate the capability of the present CACE LBE, where the two wettable cylindrical particles are freely floating at the fluid-fluid interface. As shown in the previous subsection, when the particle's weight or the gravity force is ignored, the fluid-fluid interface maintains a flat shape at equilibrium. However, when the particle's weight cannot be neglected with $\rho_p \neq \rho$, the fluid-fluid interface becomes deformed in the presence of gravity. This deformed interface can induce the capillary interactions between particles trapped at the same fluid-fluid interface. In this work, three simulations are carried out to investigate the capillary interactions between two wettable cylindrical particles in a physical domain $2L \times 2L$: (1) two identical heavy-weight particles, (2) two identical light-weight particles, and (3) one heavy-weight particle and one light-weight particle, where the particles are trapped at the fluid-fluid interface and freely move in the vertical direction.

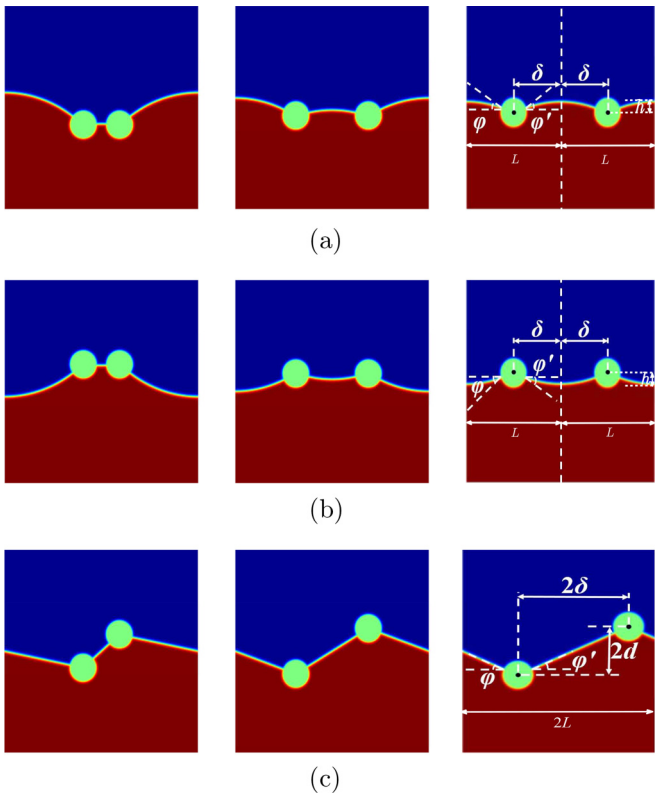

FIG. 4. Snapshots of the mechanical equilibrium state for the capillary interaction between two cylindrical particles trapped at the deformable fluid-fluid interface with δ varied from $24\delta x$ to $64\delta x$ at $|\mathrm{Bo}| = 0.257$ and contact angle $\theta = \pi/2$. (a) $\rho_{p1} = \rho_{p2} = 1.5$, (b) $\rho_{p1} = \rho_{p2} = 0.5$ and (c) $\rho_{p1} = 1.5$, $\rho_{p2} = 0.5$. φ and φ' are the slope angle of the fluid-fluid interface at the contact point between the interface and particle surface. δ is the distance of the mass center of the cylindrical particle to the vertical center line of the physical domain, h is the downward displacement from the fluid-fluid interface to the cylindrical particle center, d is the half vertical separation distance between the two cylindrical particles, and L is the half distance of physical domain in horizontal direction. From left to right columns correspond to $\delta = 24\delta x, 48\delta x, 64\delta x$, respectively.

Initially, the horizontal flat interface of the two immiscible fluids separates the physical domain equally with upper fluid density ρ_g and lower fluid density ρ_l, and the distance of the mass center of two particles to the vertical center line of the physical domain is δ as shown in Fig. 4. The two wettable cylindrical particles experience a capillary force (lateral force) F^{lat} in the horizontal direction during the particles reaching a vertically stable equilibrium position under gravity. When the system reaches a mechanically equilibrium state, the force balance at the contact point gives the following analytical expression for the capillary force in the horizontal direction [31]:

$$F^{\mathrm{lat}} = \sigma[\cos\varphi - \cos\varphi'] + R_p\Big[-\sin\Big(\frac{\pi}{2} - \theta + \varphi\Big) + \sin\Big(\frac{\pi}{2} - \theta + \varphi'\Big)\Big]\delta p, \tag{27}$$

where φ and φ' are the slope angle of the fluid-fluid interface at the contact point between the interface and particle surface as shown in Fig. 4, δp is the pressure difference between the two immiscible fluids.

In the simulation, the computational domain is divided into a 256×256 grid with the same boundary conditions as the previous case. The properties of the fluids and cylindrical particles are given by $\rho_l = \rho_g = 1$, $\eta_l/\eta_g = 1.0$, and $(\rho_{p1}, \rho_{p2}) = (1.5, 1.5)$, $(0.5, 0.5)$, and $(1.5, 0.5)$ for cases (1), (2), and (3), respectively, and Bond number $|\mathrm{Bo}| = 0.257$ [$\mathrm{Bo} = (\rho_p - \rho)R_p^2 g/\sigma$]. The other input parameters are the same as the previous test. Initially, the mass center of cylindrical particles with radius $R_p = 20$ is trapped at the fluid-fluid interface. The mechanical equilibrium state of the two cylindrical particles trapped at the fluid-fluid interface is shown in Fig. 4 with neutral wetting particle and the distance 2δ between the mass center of the cylindrical particles varied from $48\delta x - 128\delta x$. In case (1), the two heavy cylindrical particles immerse into the lower fluid region, and the two cylindrical particles will immerse into the upper fluid region in case (2), while one heavy cylindrical particle immerses into the lower fluid region and one light cylindrical particle immerses into the upper fluid region in case (3). From Fig. 4, it can be found qualitatively that the heavy (light) cylindrical particles will immerse into the lower (upper) fluid region deeper with small δ than that with large one in case (1) [case (2)], while the vertical separation $2d$ of the two cylindrical particles in case (3) is increased with δ. To give a quantitative comparison, the equilibrium cylindrical particle position is measured and compared with the theoretical prediction in Ref. [31] for different contact angle θ and δ in Fig. 5(a). It is observed that the magnitude of the downward displacement $h/\delta x$ is decreased with the increase of θ or δ in case (1), but with an opposite trend in case (2). For case (3), the vertical separation d is increased with δ, but the numerical predictions are almost overlapped by different contact angle as shown in Fig. 5(a). This implies that it is not sensitive to the value of particle wettability for case (3), which is consistent with the theoretical prediction by Ref. [31]. The results also show that numerical predictions by the present LBE agree well with the theoretical ones. We further measured the capillary force in the horizontal direction for cases (1) and (3) in Fig. 5(b), and the results show that the magnitude of F^{lat} is strengthened with small δ and it becomes negligible at $\delta = 64\delta x$ due to the symmetric capillary interactions in the two cylindrical particle fluid-solid system. Similar to the results of cases (1) and (3) in Fig. 5(a), the magnitude of F^{lat} is decreased with the increase of θ or δ in case (1), and it is not sensitive to the value of particle wettability in case (3), where the numerical predictions are almost overlapped. This can be explained from Eq. (27), where the zero curvature for the fluid-fluid interface in case (3) gives $\delta p = 0$ and causes an independent contact angle θ lateral force F^{lat}. The theoretical predictions are plotted in Fig. 5(b) for the further validation of the present LBE together with the subplot for $\rho_{p1} = \rho_{p2} = 1.5$; it is clearly shown that the present measured value of F^{lat} agrees with the theory.

C. Sinking of a horizontal cylinder through an air-water interface

Now the sinking of a horizontal cylinder through an air-water interface is carried out to show the capability of the

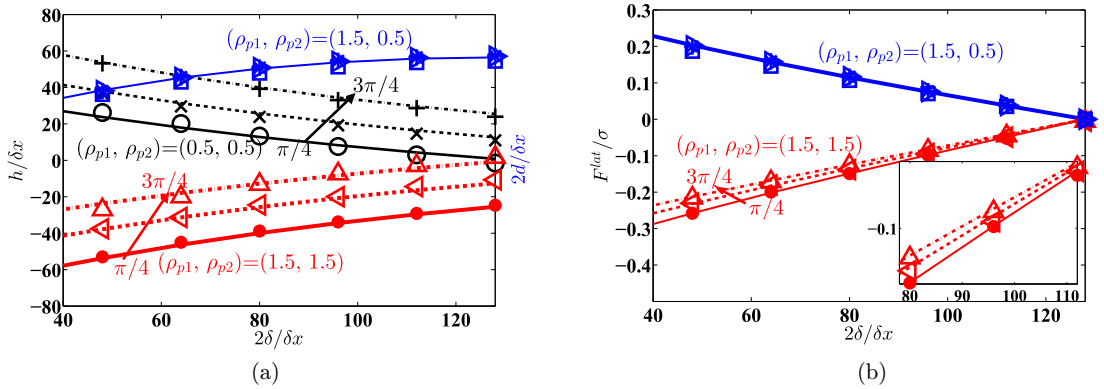

FIG. 5. Comparison of numerical predictions in cases (1)–(3) by the present LBE and the theory for two cylindrical particles trapped at the fluid-fluid interface under the gravity with contact angle varied from $\pi/4$ to $3\pi/4$. (a) Downward displacement $h/\delta x$ and vertical separation $2d/\delta x$; (b) lateral force F^{lat} between two cylindrical particles trapped at the fluid-fluid interface. Lines are theoretical results [31], and samples are numerical predictions. •, ◁, and △ are for contact angle $\pi/4$, $\pi/2$, and $3\pi/4$, respectively, with $\rho_{p1} = \rho_{p2} = 1.5$; ○, ×, and + are present for contact angle $\pi/4$, $\pi/2$ and $3\pi/4$ respectively with $\rho_{p1} = \rho_{p2} = 0.5$; and □, ∗, and ▷ are present for contact angle $\pi/4$, $\pi/2$, and $3\pi/4$ respectively with $\rho_{p1} = 1.5$, $\rho_{p2} = 0.5$.

present LBE for capturing the moving contact line with large density contrast. This two-dimensional problem is widely studied experimentally [41] and numerically [42,43]. As shown in Fig. 6, half of the cylinder with diameter D_c is immersed into the water and trapped at the air-water interface. The characteristic time and length of this problem are chosen as the experiment work [41] $t_c = (\sigma/\rho_l g^3)^{1/4}$ and $l_c = (\sigma/\rho_l g)^{1/2}$, where g is the acceleration of gravity. Initially, the cylinder is stationary, then it starts to move by gravity as in Ref. [41]. The physical domain of this problem is chosen as $12D_c \times 5D_c$, which is sufficiently wide to neglect the effect of the capillary wave reflected by the cylinder. The nonslip boundary condition is applied to the top and bottom walls, and the periodic boundary condition is used in the horizontal direction. In the simulation, the center of cylinder with $D_c = 100$ is initially located at $0.0352l_c$ below the air-water interface, which is beneath the top wall with D_c. The input parameters are chosen close to the experiment [41] as the density ratio of water and air $\rho_r = 772$ and viscosity ratio 50, $\rho_p/\rho_l = 1.92$, the wettability of the cylinder set by $\theta = 111^\circ$, Reynolds number Re = 250, Bond number Bo = 0.8649, and Weber number We = 0.93. The snapshots of the sinking dynamics predicted by the present LBE and the experimental results are compared in Fig. 7. The results show that the sinking dynamics of the cylinder is captured qualitatively by the present LBE, which agrees with the experimental results at different time series $t = 0.02$ s, 0.04 s, 0.06 s, and 0.102 s. In Fig. 8, the quantitative comparisons of the angle of the contact line position to the mass center of the cylinder and the nondimensional position of the cylinder relative to the air-water interface denoted by β and H, respectively, are plotted against the nondimensional time $T = t/t_c$. It is shown that the angle of the contact line and the positions of sinking cylinder predicted by the present LBE agree with the experimental data [41]. Moreover, the case of the cylinder centered above the undeformed air-water interface is carried out for further validation, and the time evolution of H is measured, where $\rho_p/\rho_l = 3.13$, Bo = 0.3136, and We = 0.56. Initially, the center of the cylinder is located at $0.3412l_c$ above the air-water interface. The numerical prediction of the nondimensional

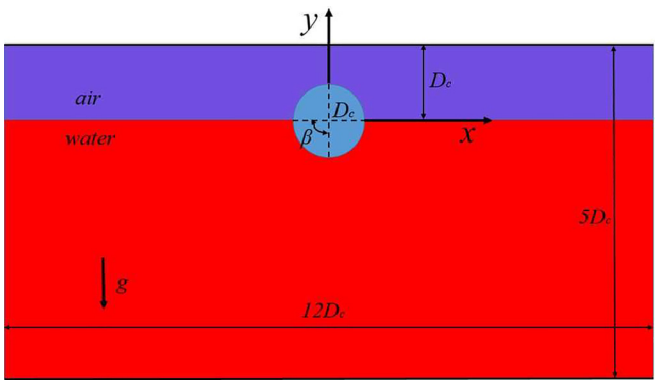

FIG. 6. Physical configuration for sinking of a horizontal cylinder through an air-water interface.

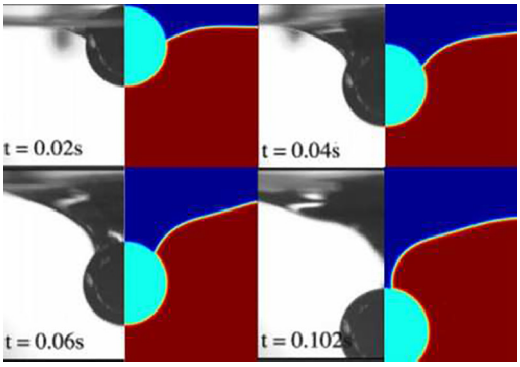

FIG. 7. Snapshots of a circular cylinder sinking dynamics through an air-water interface. The left and right halves in the subfigures are the results of experiment [41] and the present work, respectively. Adopted with permission from [41], copyright © 2006 American Chemical Society.

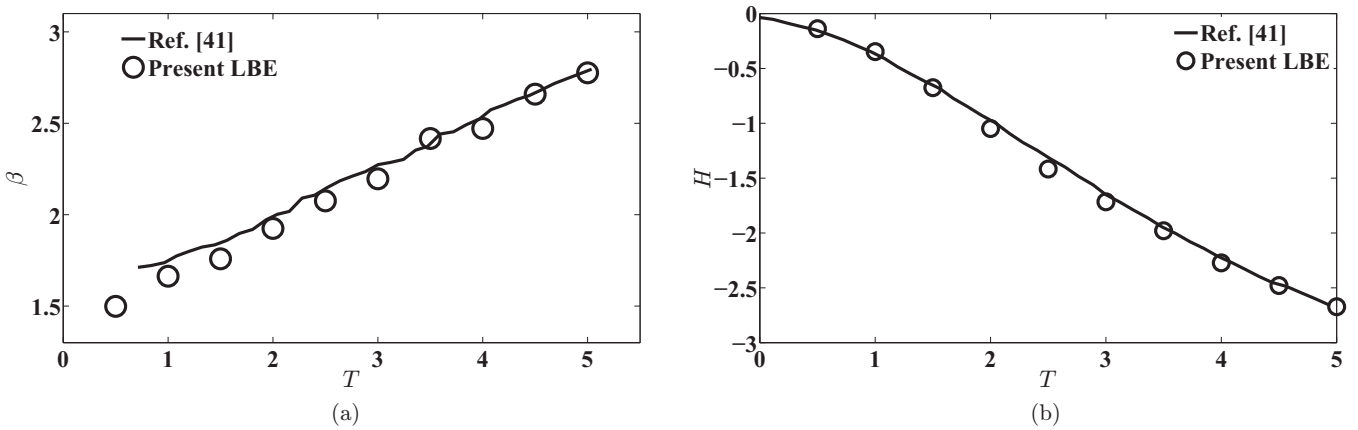

FIG. 8. Comparison of (a) the angle of contact line and (b) the position of the sinking cylinder between the present LBE and experimental data [41].

position of the cylinder is shown in Fig. 9 together with the experimental data; it is observed that numerical predictions by the present LBE agree with the experimental data [41].

D. Raft sinking of multiple horizontal cylinders through an air-water interface

In the fluid-fluid-solid multiphase system, the vertical component of capillary force acting on the solid particle can make it float at the fluid-fluid interface even with heavier solid particles than in either fluid phase. When more additional particles are present, the particles will cluster together by the horizontal component of capillary force. During the cluster process, the particles move toward each other, and the interior meniscus between the two particles may become small. This cause a diminished vertical capillary force from the meniscus acting on the solid particle, which induces the raft sinking of multiple solid particles. This interesting phenomenon was studied by theory [44] and experiment [45]. In Fig. 10 the maximum weight $M_{p,max}$ of a single horizontal cylinder with another one floating at the air-water interface is investigated with (Bo, We) = (0.25, 0.5) and (0.7225, 0.85), respectively, where the two identical horizontal cylinders are separated by 2δ as shown in Fig. 4(a). The property of air-water is same as the case in Sec. IV C. The results show that $M_{p,max}$ is diminished when two horizontal cylinders get closer. This implies that the existence of an additional horizontal cylinder can cause a sinking when they approach each other, which is consistent with the work in Ref. [44].

Finally, we conduct an additional simulation to show the capability of the present LBE for raft sinking of two, three, and five horizontal cylinders through the air-water interface. The physical configuration is the same as Fig. 6 except for more additional cylinders, where the cylinders are symmetrically distributed at the air-water interface with respect to the vertical center line of the domain and a uniform gap D_c is imposed between the cylinder and its neighboring ones at the beginning. In the simulation, the input parameters are the same as the case in Sec. IV C except for Bo = 0.7225 and We = 0.85. Figure 11 shows the snapshots of raft sinking of the cylinders through the air-water interface at different nondimensional time series. At the early stage, the cylinders are pulled together by the capillary force. As the time goes on, the gap and the interior meniscus between cylinders become small. When the capillary force cannot support the cylinders in the floating at air-water interface, the raft sinking of the cylinders is observed at a later stage. Similar raft sinking phenomena were also observed in Refs. [43,45]. The

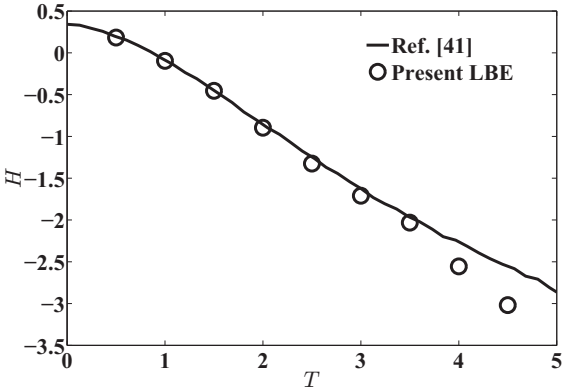

FIG. 9. Comparison of the position of sinking cylinder between the present LBE and experimental data [41].

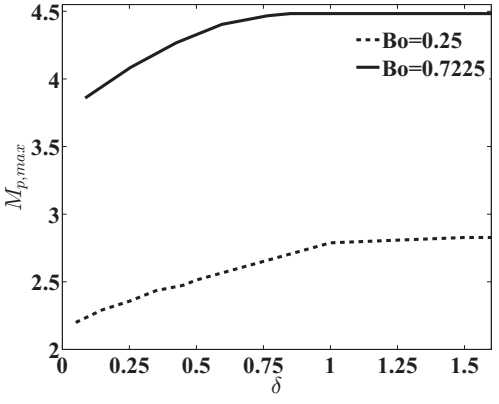

FIG. 10. Maximum weight of horizontal cylinder vs δ that makes the cylinder float at the air-water interface with (Bo, We) = (0.25, 0.5) and (0.7225, 0.85).

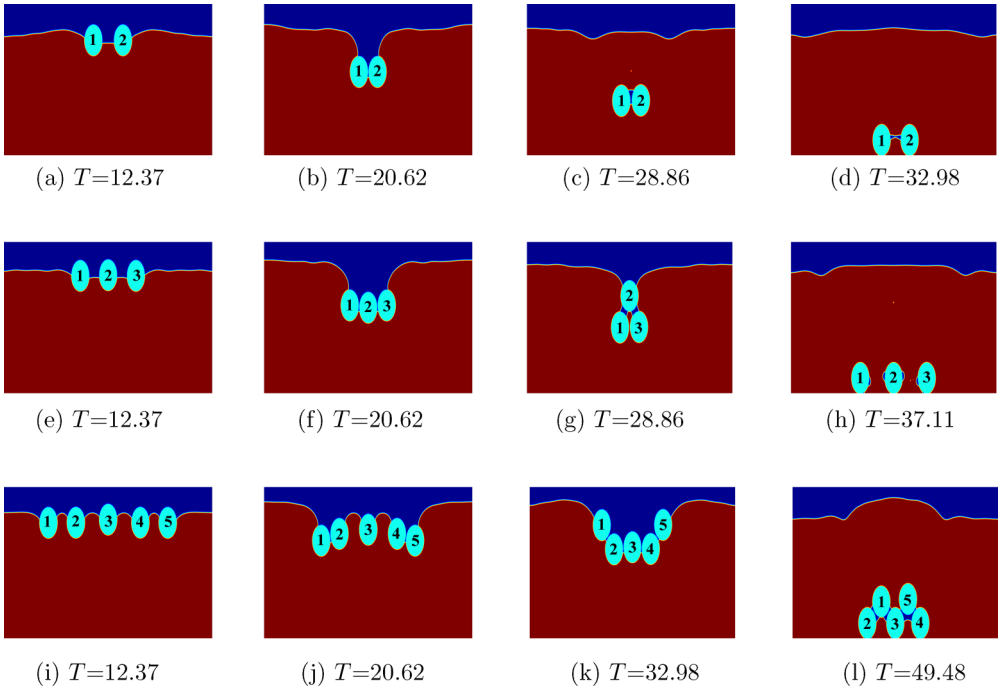

FIG. 11. Snapshots of raft sinking of two, three, and five circular cylinders through the air-water interface. (a)–(d) Two circular cylinders, (e)–(h) three circular cylinders, (i)–(l) five circular cylinders.

quantitative motion of the initial position of the first cylinder from the left side vs time T is presented in Fig. 12 as an example to show the raft sinking process. The horizontal position in Fig. 12(a) shows that the first cylinder distributed initially at the left side gradually moves to the center of the domain, and it reaches a maximum value and then it starts to leave the central region and reach a stable position. During the horizontal position approaching the maximum value, the horizontal cylinder floats up and down as its vertical position shown in Fig. 12(b). After that, the cylinder starts to sink. For example, the sinking of the cylinder starts at time around $T =$ 20, 30, and 45, respectively for the raft sinking of two, three, and five horizontal cylinders through an air-water interface. Moreover, the normalized position of the raft sinking of three and five horizontal cylinders vs time T is plotted in Fig. 13 together with the overall mass center (x_{av}, y_{av}) of multiple horizontal cylinders. The results in Fig. 13(a) and 13(c) further show that the cylinders first approach the central region and then separate to their stable positions. The vertical position y_p of the multiple horizontal cylinders in Figs. 13(b) and 13(d) demonstrates that an unusual nonmonotonic motion of the multiple horizontal cylinders is observed in the vertical plane rather than the sinking of a horizontal cylinder with a monotonic descent motion in Sec. IV C. However, the overall mass center of multiple horizontal cylinders x_{av} is almost along the centerline of the domain, while y_{av} is a nonmonotonic motion

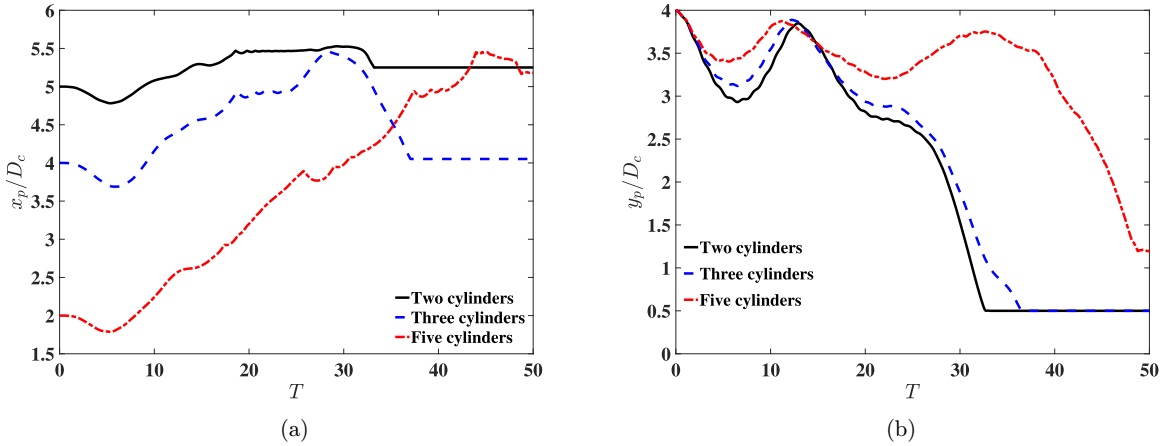

FIG. 12. Normalized position of the first cylinder distributed initially at the left side in the raft sinking of multiple horizontal cylinders vs time T. (a) Horizontal position x_p; (b) vertical position y_p.

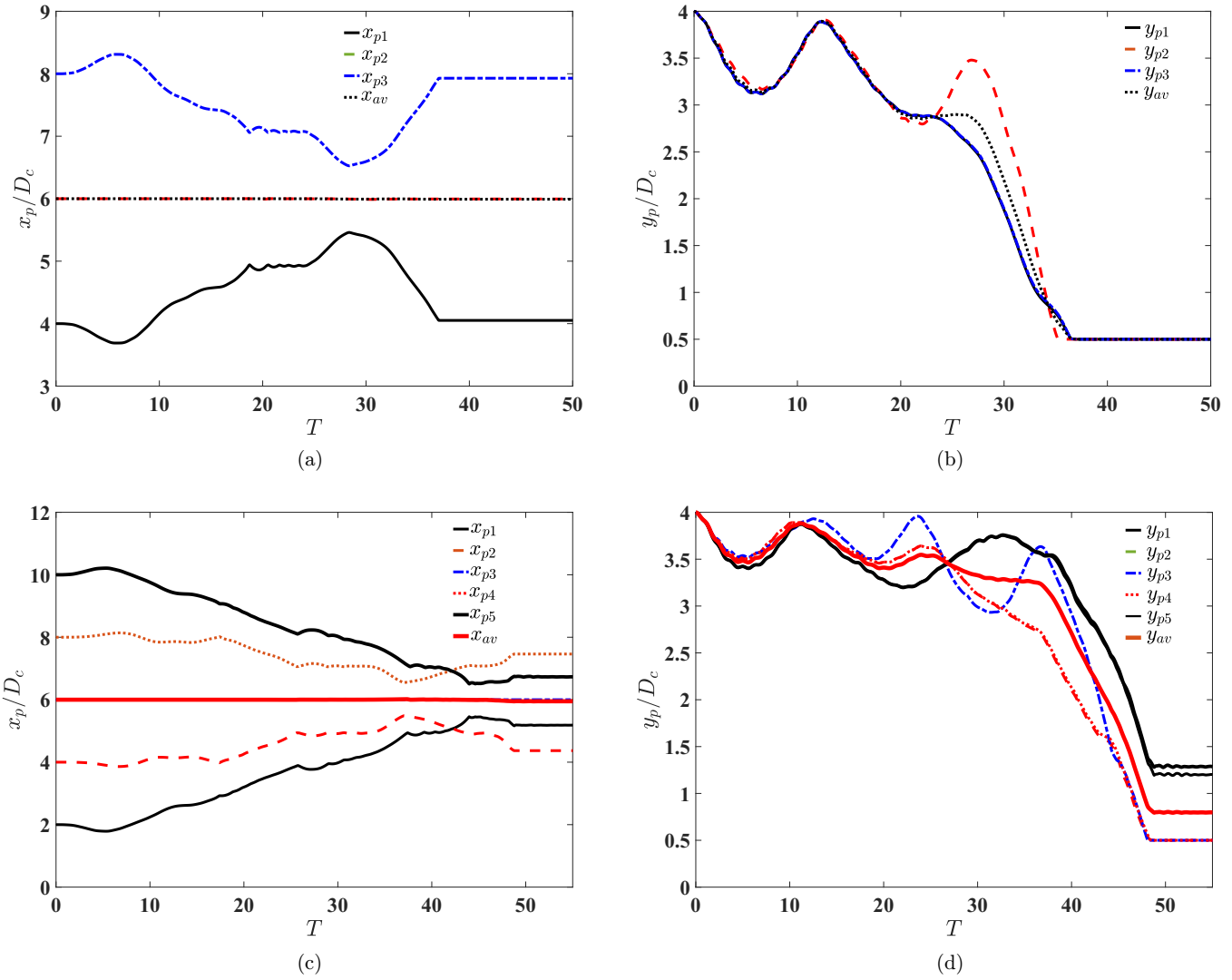

FIG. 13. Normalized position of the raft sinking of three and five horizontal cylinders vs time T together with the overall mass center (x_{av}, y_{av}) of multiple cylinders. (a), (c) Horizontal position x_p; (b), (d) vertical position y_p.

as the motion of an individual horizontal cylinder in the raft sinking of multiple horizontal cylinders.

V. CONCLUSION

In this work a phase-field based LBE is developed for wettable particle hydrodynamics with a large fluid properties contrast. The flow field is calculated by classical incompressible LBE, and the evolution of the fluid-fluid interface is captured by CACE LBE. Due to the merit of the SPM for describing the particle and computing the fluid-solid interaction force, the solid particle is represented by the SPM and the fluid-solid interaction force is calculated by the direct force method. However, the diffusion problem between the wettable solid and surrounding fluids occurs in the present SPM-LBE when the wettable particle immerses into two immersible fluids. Then a remedial strategy is introduced to solve this problem.

Some classical problems including a single wettable particle trapped at the fluid-fluid interface without gravity, capillary interactions between two wettable particles under gravity, and sinking of a horizontal cylinder through an air-water interface were carried out to validate the capability and accuracy of the present LBE for fluid-fluid-solid three-phase flows. All numerical results showed that the predictions of the wettable particles hydrodynamics by the present LBE agreed with analytical solutions and available experimental data. Moreover, the phenomena of raft sinking of multiple circular cylinders were observed by the present SPM-LBE. Numerical results showed that an unusual nonmonotonic motion of the multiple horizontal cylinders was observed in the vertical plane rather than a monotonic descent motion by sinking of a horizontal cylinder.

ACKNOWLEDGMENTS

This work is supported by the National Natural Science Foundation of China (Grant No. 51876092), the Natural Science Foundation of Zhejiang Province (Grant No. LY21E060010), First Class Discipline of Zhejiang A (Zhejiang University of Finance and Economics-Statistics), First

Class Discipline B (Mathematics) Funding for Zhejiang University of Finance and Economics, the Collaborative Innovation Center for Data Science and Big Data Analysis (Zhejiang University of Finance and Economics-Statistics).

[1] G. Tryggvason, B. Bunner, A. Esmaeeli, D. Juric, N. Al-Rawahi, W. Tauber, J. Han, S. Nas, and Y.-J. Jan, A front-tracking method for the computations of multiphase flow, J. Comput. Phys. **169**, 708 (2001).

[2] Y. C. Chang, T. Y. Hou, B. Merriman, and S. Osher, A level set formulation of Eulerian interface capturing methods for incompressible fluid flows, J. Comput. Phys. **124**, 449 (1996).

[3] D. Gueyffier, J. Li, A. Nadim, R. Scardovelli, and S. Zaleski, Volume of fluid interface tracking with smoothed surface stress methods for three-dimensional flows, J. Comput. Phys. **152**, 423 (1999).

[4] D. Anderson, G. McFadden, and A. Wheeler, Diffusive-interface methods in fluid mechanics, Annu. Rev. Fluid Mech. **30**, 139 (1998).

[5] A. K. Gunstensen, D. H. Rothman, S. Zaleski, and G. Zanetti, Lattice Boltzmann model of immiscible fluid, Phys. Rev. A **43**, 4320 (1991).

[6] X. Shan and H. Chen, Lattice Boltzmann model for simulating flows with multiple phases and components, Phys. Rev. E **47**, 1815 (1993).

[7] X. He, S. Chen, and R. Zhang, A lattice Boltzmann scheme for incompressible multiphase flow and its application in simulation of Rayleigh-Taylor instability, J. Comput. Phys. **152**, 642 (1999).

[8] L. S. Luo, Theory of the lattice Boltzmann method: Lattice Boltzmann models for nonideal gases, Phys. Rev. E **62**, 4982 (2000).

[9] Z. L. Guo and T. S. Zhao, Finite-difference-based lattice Boltzmann model for dense binary mixtures, Phys. Rev. E **71**, 026701 (2005).

[10] T. Lee and P. F. Fischer, Eliminating parasitic currents in the lattice Boltzmann equation method for nonideal gases, Phys. Rev. E **74**, 046709 (2006).

[11] T. Lee and C. L. Lin, A stable discretization of the lattice Boltzmann equation for simulation of incompressible two-phase flows at high density ratio, J. Comput. Phys. **206**, 16 (2005).

[12] T. Lee and L. Liu, Lattice Boltzmann simulations of micron-scale drop impact on dry surfaces, J. Comput. Phys. **229**, 8045 (2010).

[13] S. Leclaire, M. Reggio, and J. Trepanier, Progress and investigation on lattice Boltzmann modeling of multiple immiscible fluids or components with variable density and viscosity ratios, J. Comput. Phys. **246**, 318 (2013).

[14] L. Zheng, S. Zheng, and Q. L. Zhai, Lattice Boltzmann equation method for the Cahn-Hilliard equation, Phys. Rev. E **91**, 013309 (2015).

[15] M. Geier, A. Fakhari, and T. Lee, Conservative phase-field lattice Boltzmann model for interface tracking equation, Phys. Rev. E **91**, 063309 (2015).

[16] H. L. Wang, Z. H. Chai, B. C. Shi, and H. Liang, Comparative study of the lattice Boltzmann models for Allen-Cahn and Cahn-Hilliard equations, Phys. Rev. E **94**, 033304 (2016).

[17] F. Ren, B. W. Song, M. C. Sukop, and H. B. Hu, Improved lattice Boltzmann modeling of binary flow based on the conservative Allen-Cahn equation, Phys. Rev. E **94**, 023311 (2016).

[18] A. Fakhari and D. Bolster, Diffuse interface modeling of three-phase contact line dynamics on curved boundaries: A lattice Boltzmann model for large density and viscosity ratios, J. Comput. Phys. **334**, 620 (2017).

[19] H. L. Wang, X. L. Yuan, H. Liang, Z. H. Chai, and B. C. Shi, A brief review of the phase-field-based lattice Boltzmann method for multiphase flows, Capillarity **2**, 33 (2019).

[20] L. Zheng, S. Zheng, and Q. L. Zhai, Multiphase flows of *N* immiscible incompressible fluids: Conservative Allen-Cahn equation and lattice Boltzmann equation method, Phys. Rev. E **101**, 013305 (2020).

[21] L. Zheng, S. Zheng, and Q. L. Zhai, Reduction-consistent phase-field lattice Boltzmann equation for *N* immiscible incompressible fluids, Phys. Rev. E **101**, 043302 (2020).

[22] A. J. C. Ladd, Numerical simulations of particulate suspensions via a discretized Boltzmann equation. Part 1. Theoretical foundation, J. Fluid Mech. **271**, 285 (1994).

[23] P. Lallemand and L. S. Luo, Lattice Boltzmann method for moving boundaries, J. Comput. Phys. **184**, 406 (2003).

[24] O. Filippova and D. Hänel, Grid refinement for lattice-BGK models, J. Comput. Phys. **147**, 219 (1998).

[25] D. Yu, R. Mei, and W. Shyy, A unified boundary treatment in lattice Boltzmann method, in *Proceedings of the 41st Aerospace Sciences Meeting and Exhibit 2003, Reno, NV* (AIAA, Reston, VA, 2003), paper no. 2003–953.

[26] Y. Nakayama and R. Yamamoto, Simulation method to resolve hydrodynamic interactions in colloidal dispersions, Phys. Rev. E **71**, 036707 (2005).

[27] S. Jafari, R. Yamamoto, and M. Rahnama, Lattice-Boltzmann method combined with smoothed-profile method for particulate suspensions, Phys. Rev. E **83**, 026702 (2011).

[28] Z. Hashemi, S. Jafari, and M. Rahnama, Comparative study of momentum-exchange and smoothed profile methods in lattice Boltzmann method, Comput. Fluids **100**, 65 (2014).

[29] Y. K. Lee and K. H. Ahn, A novel lattice Boltzmann method for the dynamics of rigid particles suspended in a viscoelastic medium, J. Non-Newtonian Fluid Mech. **244**, 75 (2017).

[30] J. Liu, C. S. Huang, Z. H. Chai, and B. C. Shi, A diffuse-interface lattice Boltzmann method for fluid-particle interaction problems, Comput. Fluids **233**, 105240 (2022).

[31] Y. Mino and H. Shinto, Lattice Boltzmann method for simulation of wettable particles at a fluid-fluid interface under gravity, Phys. Rev. E **101**, 033304 (2020).

[32] Y. K. Lee and K. H. Ahn, Particle dynamics at fluid interfaces studied by the color gradient lattice Boltzmann method coupled with the smoothed profile method, Phys. Rev. E **101**, 053302 (2020).

[33] K. W. Connington, T. Lee, and J. F. Morris, Interaction of fluid interfaces with immersed solid particles using the lattice

Boltzmann method for liquid-gas-particle systems, J. Comput. Phys. **283**, 453 (2015).

[34] X. He and D. Doolen, Lattice Boltzmann method on curvilinear coordinates systems: Flow around a circular cylinder, J. Comput. Phys. **134**, 306 (1997).

[35] J. W. Cahn and J. E. Hilliard, Free energy of a nonuniform system. I. Interfacial free energy, J. Chem. Phys. **28**, 258 (1958).

[36] S. M. Allen and J. W. Cahn, Mechanisms of phase transformations within the miscibility gap of Fe-rich Fe-Al alloys, Acta Metall. **24**, 425 (1976).

[37] P. H. Chiu and Y. T. Lin, A conservative phase field method for solving incompressible two-phase flows, J. Comput. Phys. **230**, 185 (2011).

[38] L. Zheng, S. Zheng, and Q. L. Zhai, Continuous surface force based lattice Boltzmann equation method for simulating thermocapillary flow, Phys. Lett. A **380**, 596 (2016).

[39] D. Iwahara, H. Shinto, M. Miyahara, and K. Higashitani, Liquid drops on homogeneous and chemically heterogeneous surfaces: A two-dimensional lattice Boltzmann study, Langmuir **19**, 9086 (2003).

[40] Z. L. Guo, C. G. Zheng, and B. C. Shi, Force imbalance in lattice Boltzmann equation for two-phase flows, Phys. Rev. E **83**, 036707 (2011).

[41] D. Vella, D. G. Lee, and H. Y. Kim, Sinking of a horizontal cylinder, Langmuir **22**, 2972 (2006).

[42] H. R. Liu, P. Gao, and H. Ding, Fluid-structure interaction involving dynamic wetting: 2D modeling and simulations, J. Comput. Phys. **348**, 45 (2017).

[43] A. O'Brien and M. Bussmann, A moving immersed boundary method for simulating particle interactions at fluid-fluid interfaces, J. Comput. Phys. **402**, 109089 (2020).

[44] D. Vella, P. D. Metcalfe, and R. J. Whittaker, Equilibrium conditions for the floating of multiple interfacial objects, J. Fluid Mech. **549**, 215 (2006).

[45] M. Abkarian, S. Protière, J. M. Aristoff, and H. A. Stone, Gravity-induced encapsulation of liquids by destabilization of granular rafts, Nat. Commun. **4**, 1895 (2013).